THE ASTROPHYSICAL JOURNAL, 458:653–669, 1996 February 20

FAR OUTER GALAXY H II REGIONS

ALEXANDER L. RUDOLPH,[1,2] JAN BRAND,[3] EUGÈNE J. DE GEUS,[4,5] AND JAN G. A. WOUTERLOOT[6]

Received 1994 June 8; accepted 1995 August 29

ABSTRACT

We have made a multiwavelength (6, 3.6, and 2 cm), high-resolution (3″–6″) radio continuum survey of *IRAS*-selected sources to search for and study H II regions in the far-outer Galaxy. We identified 31 sources with $R \gtrsim 15$ kpc and $L_{\rm FIR} \gtrsim 10^4\ L_\odot$, indicating the presence of high-mass star formation.

We have observed 11 of these sources with the Very Large Array (VLA). The 6 and 2 cm observations were made using "scaled arrays," making possible a direct and reliable determination of spectral indices. Of the 39 sources we detected at 6 cm, 10 have spectral indices consistent with optically thin free-free emission from H II regions and are within 45″ of the associated *IRAS* source. Combining our data with previous VLA observations by other investigators we analyzed a sample of 15 of the most remote H II regions found in our Galaxy, located at $R = 15$–18.2 kpc.

The sizes of the H II regions range from $\lesssim$0.10 to 2.3 pc. Using the measured flux densities and sizes, we determined their electron densities, emission measures, and excitation parameters, as well as their Lyman continuum fluxes needed to keep the nebulae ionized. The sizes and electron densities indicate that most of the sources are (ultra)compact H II regions.

Seven of the 15 H II regions have sizes $\lesssim$0.20 pc. The large number of compact H II regions suggests that the time these regions spend in a compact phase must be much longer than their dynamical expansion times.

Five of the 15 H II regions have cometary shapes; the remainder are spherical or unresolved. Comparison of our data with molecular line maps suggests that the cometary shape of the two H II regions in S127 may be due to pressure confinement of the expanding ionized gas, as in the "blister" or "champagne flow" models of H II regions. Comparison of our data with the *IRAS* data indicates that the five most luminous H II regions are consistent with a single zero-age main sequence O or B star exciting a dust-free H II region.

Subject headings: H II regions — ISM: individual (S127) — radio continuum: ISM — surveys — stars: formation

1. INTRODUCTION

Studying the details of massive star formation under physical circumstances different from those in the solar neighborhood and inner Galaxy is important for obtaining a complete picture of star formation in the Milky Way, as well as for understanding star formation in galaxies other than our own. The ideal locations for investigating these differences are the molecular clouds at the outer edge of our own Galaxy. The distances of these objects from the Galactic center are large enough for the properties of the interstellar medium to be significantly different from those inside the solar circle. The average gas density is lower, molecular clouds are more sparsely distributed (Wouterloot et al. 1990), the diffuse Galactic 100 μm emission is weaker (Bloemen, Deul, & Thaddeus 1990), the metallicity may be lower (Shaver et al. 1983; Fich & Silkey 1991; Wilson & Matteucci 1992; Rudolph et al. 1996), and yet the objects are near enough to allow us to resolve small-scale structures and to identify individual stars.

An H II region is the result of the interaction between a recently formed high-mass star and the surrounding neutral interstellar medium (ISM). By ionizing and heating the surrounding gas and dust, an O or B star announces its presence in a way that can be studied over extremely large distances. Thus, H II regions are prime sites to study star formation throughout the entire Galaxy, as well as in other galaxies. Radio continuum observations can provide information on the electron density, excitation, and stellar content of the region.

Fich (1986) mapped with the VLA all 135 unresolved radio sources in the range $l = 93°$–$163°$ and $b = -4°$ to $+4°$, stronger than 0.3 Jy in the 10′ resolution radio survey of Kallas & Reich (1980, hereafter KR). The distance to most of these sources is not known. Other radio surveys of H II regions have focused on optical H II regions (Felli & Harten 1981; Fich 1993, hereafter F93), known Galactic radio sources (Wink, Wilson, & Bieging 1983; Caswell & Haynes 1987; Wood & Churchwell 1989, hereafter WC), or *IRAS*-selected sources (McCutcheon et al. 1991; Kurtz, Churchwell, & Wood 1994), but have not specifically concentrated on the outer Galaxy. A number of studies of outer Galaxy star-forming regions have included radio continuum observations (Wouterloot, Brand, & Henkel 1988a, hereafter WBH; Mead, Kutner, & Evans 1990; Carpenter, Snell, & Schloerb 1990), but have not selected their sources systematically.

Surveys based on optical H II regions are biased toward nearby objects due to extinction. Thus, to search for H II regions in the far-outer Galaxy, we have made a radio continuum survey of sources selected from the catalog of Wouterloot & Brand (1989, hereafter WB89), who observed CO emission from a large number of *IRAS* point sources and derived their kinematic distances. A search for H_2O maser emission from

[1] NASA/Ames Research Center, Mail Stop 245-6, Moffett Field, CA 94035-1000.
[2] Department of Physics, Harvey Mudd College, Claremont, CA 91711.
[3] Istituto di Radioastronomia, CNR, Via Gobetti 101, I-40129 Bologna, Italy.
[4] Department of Astronomy, University of Maryland, College Park, MD 20742.
[5] Present address: Astronomy Department, Caltech 105-24, Pasadena, CA 91125.
[6] I. Physikalisches Institut, Zülpicher Strasse 77, D-50937 Köln, Germany.

TABLE 1A

OBSERVED OUTER GALAXY FIELDS OF VIEW

Catalog Name	*IRAS* Name	l[a]	b	R (kpc)	d_{kin} (kpc)	$L_{FIR}/10^4$ ($L_\odot$)
WB 85[b]	21270+5423	96°29	2°59	15.0	11.5	10.0
WB 145	21569+5923	102.63	3.76	14.9	10.5	1.2
WB 361	00453+6414	122.60	1.64	18.2	12.2	1.3
WB 380	01045+6505	124.64	2.54	17.0	10.7	11.0
WB 391	01160+6529	125.80	3.05	16.9	10.5	1.1
WB 399[c]	01420+6401	128.78	2.01	16.8	10.1	4.4
WB 414	02071+6235	131.86	1.33	16.8	9.9	1.1
WB 436[c]	02383+6241	135.18	2.69	16.1	9.0	3.8
WB 437	02395+6244	135.28	2.80	16.2	9.1	7.1
WB 440	02421+6233	135.63	2.76	16.4	9.3	2.0
WB 529	04025+5313	149.59	0.90	19.0	11.2	1.8

[a] Due to a bug in the program used by WB89 to convert R.A. and decl. to l and b, the corrected values of l in this table differ slightly from those in WB89.

[b] WB 85 is associated with the optical H II region S127 (see Table 1B).

[c] WB 399 and WB 436 are associated with optical nebulosities identified in this paper.

many of these sources has been made by Wouterloot, Brand, & Fiegle (1993), and the molecular clouds associated with 27 sources located at $R \gtrsim 16$ kpc were studied by Brand & Wouterloot (1994, 1995).

We have used the VLA to observe 11 far-outer Galaxy sources (typical heliocentric distances ≈ 10 kpc; $R \gtrsim 15$ kpc). The resolution of these observations (3″–6″) makes possible a comparison of the distribution of the ionized gas with millimeter interferometric maps of the associated molecular clouds (de Geus et al. 1996).

2. SOURCE SELECTION

Wouterloot & Brand (1989; WB89) made an extensive CO survey toward *IRAS* point sources located mostly in the second and third Galactic quadrants ($85° < l < 280°$). Their selection criteria were based on the sources' infrared colors and discriminate in favor of sources frequently associated with H_2O masers and dense molecular cloud "cores," i.e., where star formation is currently taking place (Wouterloot & Walmsley 1986; Wouterloot, Walmsley, & Henkel 1988b). Of the 1302 sources in their sample, 1077 showed CO emission from which a kinematic distance could be determined. In this paper, we use kinematic distances based on the rotation curve of Brand & Blitz (1993): $\Theta/\Theta_0 = 1.0077\ (R/R_0)^{0.0394}$ (ignoring the constant term), where Θ is circular rotation velocity and R is Galactocentric distance, and with the IAU-recommended values $R_0 = 8.5$ kpc and $\Theta_0 = 220$ km s^{-1} (Kerr & Lynden-Bell 1986). Using these distances, we converted the *IRAS* flux densities into a total infrared luminosity, including bolometric corrections.

To search for and study massive-star formation at large R, we selected the WB89 sources with $R \gtrsim 15$ kpc and $L_{FIR} \gtrsim 10^4$ $L_\odot$. The latter criterion indicates a flux of ionizing photons from a single star greater than 3×10^{46} s^{-1}, corresponding to the presence of a zero-age main sequence (ZAMS) star of spectral type earlier than B1 (Panagia 1973). Sources within 15° of $l = 180°$ tend to have large uncertainties in their kinematic distance determinations, so we rejected them, unless the distance was confirmed by association with an optical H II region with a well-determined photometric distance. These criteria resulted in 31 sources, of which 22 are easily observable from the Northern Hemisphere.

Inspection of the Palomar Observatory Sky Survey prints revealed previously unidentified nebulosities at the positions of two of the selected sources, WB 399 and WB 436, with diameters of approximately 0.′6 (1.8 pc) and 0.′8 (2.1 pc), respectively. Thus, including the known H II regions, only eight of the 22 regions are associated with optical H II regions. The other regions are optically invisible either as the result of foreground extinction or because they are too young. Our sample is not biased in extinction and, hence, provides a much larger number of sources at large R than samples based on previous optical studies. This makes our sample very well suited for follow-up studies of properties of H II regions, such as the determination of electron temperatures (using radio recombination lines) or heavy-element abundances (using ionic fine-structure lines) as a function of R (see, e.g., Shaver et al. 1983; Fich & Silkey 1991; Simpson et al. 1995; Rudolph et al. 1996).

Of the 22 regions, six with previously known optical associations have been observed at the VLA by other investigators. One source without optical association (WB 380 = IRAS 01045+6505) has also been observed at the VLA (McCutcheon et al. 1991). This paper reports on new observations of nine of the remaining 15 regions, plus repeat observations of S127 (WB 85) and WB 380, the former with higher resolution than F93. Table 1A lists the properties of these 11 regions, including their WB89 designations, *IRAS* names, Galactic coordinates, Galactocentric and heliocentric distances, and far-infrared (FIR) luminosities, while Table 1B lists these same properties for the six previously observed, optically visible regions, plus the photometric distance from Brand & Blitz (1993) where available.

3. OBSERVATIONS

Observations were made on 1992 March 8 in the "snapshot" mode in the C configuration of the VLA of the National Radio Astronomy Observatory[7] (NRAO) at 6 cm (4.8601 GHz) and 3.6 cm (8.4399 GHz). The "snapshot" durations were between 8 and 10 minutes for each of the 11 regions at both wavelengths. We observed 2146+608, 0107+562, 0224+671, or 0355+508 approximately every 45 minutes for

[7] The National Radio Astronomy Observatory is operated by Associated Universities, Inc., under contract with the National Science Foundation.

TABLE 1B

OUTER GALAXY REGIONS PREVIOUSLY OBSERVED WITH THE VLA

Catalog Name	*IRAS* Name	l	b	R (kpc)	d_{kin} (kpc)	$L_{FIR}/10^4$ ($L_\odot$)	Association	d_{phot}[a] (kpc)	Reference
WB 85	21270+5423	96°.29	2°.59	15.0	11.5	10.0	S127	7.3	1
WB 770	06084+1727	192.91	−0.62	16.0	7.6	2.8	S259	8.3	1, 2
WB 794	06158+1517	195.65	−0.11	17.8	9.4	6.4	S266	...	1, 2
WB 852	06358+0047	210.79	−2.55	14.8	6.9	1.1	S283	9.1	1, 2
WB 952	07061−0414	218.74	1.85	14.8	7.2	7.8	S288	3.0	1
WB 1006.....	07279−2038	235.69	−1.25	14.7	8.1	1.3	BBW33B[b]	5.4	2

[a] Photometric distances are from Brand & Blitz 1993.
[b] BBW = Brand, Blitz, & Wouterloot 1986.
REFERENCES.—(1) F93. (2) (WBH).

phase calibration. In addition, a 10 minute observation of 3C 48 was made at each frequency as an amplitude calibration.

Observations in the D configuration at 2 cm (14.9649 GHz) were made on 1992 September 22 in three "snapshots" of 4 minutes length each, separated by ~1 hr in time, resulting in a total integration time of 12 minutes per field of view. This strategy provides a much more complete coverage of the *u-v* plane than a single "snapshot" and thereby reduces the sidelobes of the resulting beam pattern. The negative consequence of this strategy is the additional overhead of moving the antennas, and this method is ultimately limited by the shortest time one would want to spend on the source (~4 minutes) compared to the time moving between sources (0.5–2 minutes). However, the signal-to-noise ratio of observations in the "snapshot" mode is often limited not by the on-source integration time but by the dynamic range in the map, which is determined by the size of the sidelobes in the beam. Thus, although this strategy will not be the best in all cases, it often will improve the final quality of the maps. At 2 cm, observations of 2200+420, 0016+731, 0224+671, or 0355+508 were made at regular intervals (10–25 minutes) for phase calibration, and 3C 48 was again used for the flux density calibration.

The flux densities assumed for 3C 48 were 5.635 Jy at 6 cm, 3.297 Jy at 3.6 cm, and 1.814 Jy at 2 cm, which are the standard Astronomical Image Processing System (AIPS) values and accurate to 5%. The observations at all three frequencies were made with a bandwidth of 100 MHz. Strong interference at 1435 and 1687 MHz on 1992 September 22, however, made it impossible to use the data in the second intermediate frequency (IF) of the 2 cm observations, and the bandwidth actually used at 2 cm was only 50 MHz.

The data for each frequency were inspected, and bad data points were removed from the data sets. The data were then gridded, mapped, and cleaned using the AIPS routine MX. The source WB 380 contains a very bright point source at the map center, so these data were self-calibrated, leading to an improvement in the dynamic range in the maps of between factors of 4.4 (6 cm) and 1.8 (2 cm).

The maps were made at each wavelength using natural weighting, to obtain the maximum signal-to-noise ratio. The resulting resolutions are ~6″ × 5″ at 6 and 2 cm, and 3.″3 × 2.″7 at 3.6 cm. In addition, we made maps at 3.6 cm with a 40 kλ taper, giving ~6″ × 5″ resolution. The rms sensitivity in the maps is within a few percent of the theoretical sensitivity: ~0.06 mJy beam^{-1} at 6 cm, 0.05 mJy beam^{-1} at 3.6 cm, and 0.19 mJy beam^{-1} at 2 cm, except for the maps of S127 and WB 380, which are dynamic-range–limited. The flux densities were all primary-beam–corrected, although, because the H II region emission is usually within 20″–40″ of the *IRAS* positions (see § 4.1), these corrections are quite small. Table 2 summarizes the observational parameters for the three wavelengths, including the bandwidth, resolution, primary-beam size, largest observable structure, flux density calibrator, and sensitivity.

4. RESULTS

4.1. *Maps*

The maps of the 11 regions in Table 1 were inspected for emission over the entire primary beam at each of the three wavelengths. Table 3 lists the flux densities of all the sources detected at 6 cm above a 3 $\sigma \approx$ 0.18 mJy beam^{-1} level and the

TABLE 2

VLA OBSERVING PARAMETERS

Parameter	6 cm	3.6 cm	2 cm
Observation date	1992 Mar 8	1992 Mar 8	1992 Sep 22
Configuration	C	C	D
Number of antennas	27	27	27
Center frequency (GHz).....	4.8601	8.4399	14.9649
Bandwidth (MHz)	100	100	50[a]
Primary beam FWHM	9′	5.′4	3′
Synthesized beam FWHM	~5.″5	~3″(~5.″5)[b]	~5.″5
Largest structure visible[c].....	~90″	~60″	~90″
Typical rms in image (mJy beam^{-1}).....	0.06	0.05	0.19
Primary flux calibrator 3C 48 (Jy).....	5.635	3.297	1.814

[a] One of the two IF pairs was not used because of interference.
[b] The larger synthesized beam is for maps with a 40 kλ taper.
[c] These numbers are estimates and can vary depending on detailed observing strategy used.

TABLE 3

SOURCES OBSERVED AT 6 CM[a]

Source	R.A. (1950) (±^{s}.1)	Decl. (1950) (±1″)	Peak Flux (mJy beam^{-1})	Total Flux[b] (mJy)	Δ *IRAS*[c]
WB 85 A.....	21^{h}27^{m}07^s.6	54°24′22″	8.39	424	43″
B.....	21.27.04.2	54.23.20	17.76	153	26″
WB 145 A.....	21.57.30.7	59.22.54	4.6	6.0	4′.2
B.....	21.57.01.2	59.21.22	0.48	...	2′.3
WB 361 A.....	00.46.01.0	64.20.14	32	41	7′.3
B.....	00.45.21.9	64.14.21	0.54	...	5″
C.....	00.44.52.2	64.18.58	2.4	4.2	5′.7
D.....	00.44.48.7	64.14.32	13.0	17.1	3′.6
WB 380.....	01.04.36.3	65.05.22	234	295	4″
WB 391.....	01.16.03.7	65.30.02	0.52	0.61	4″
WB 399 A.....	01.42.24.9	64.04.16	2.5	...	3′.9
B.....	01.42.05.7	64.01.00	3.60	54.7	2″
C.....	01.41.25.8	64.01.18	3.2	...	4′.4
WB 414 A.....	02.07.14.0	62.37.48	0.51	1.06	2′.9
B.....	02.07.05.5	62.29.50	0.5	0.9	5′.2
C.....	02.07.04.6	62.34.33	0.18	...	33″
D.....	02.06.54.7	62.33.48	0.28	0.41	1′.9
E.....	02.06.54.2	62.33.34	0.34	...	2′.1
F.....	02.06.32.2	62.38.52	1.0	...	5′.5
G.....	02.06.17.2	62.32.38	5.4	...	6′.2
WB 436 A1.....	02.39.14.5	62.36.34	6.1	10.8	7′.5
A2.....	02.39.14.3	62.36.26	4.7		
B1.....	02.38.43.8	62.46.39	26	52	6′.0
B2.....	02.38.42.7	62.46.40	20		
C1.....	02.38.24.8	62.37.03	1.8	3.9	4′.1
C2.....	02.38.24.1	62.36.54	2.1		
D.....	02.38.22.4	62.41.20	2.49	68.4	15″
E.....	02.38.13.8	62.46.44	3.5	...	5′.7
WB 437 A.....	02.39.57.2	62.47.30	1.3	1.6	4′.4
B.....	02.39.56.8	62.44.05	0.61	1.55	3′.0
WB 440 A1.....	02.42.16.5	62.37.30	0.85	2.36	3′.8
A2.....	02.42.15.4	62.37.36	0.95		
B.....	02.42.12.6	62.34.14	0.63	...	33″
C.....	02.42.09.8	62.33.58	0.35	...	8″
D.....	02.42.09.1	62.33.44	0.24	...	9″
E.....	02.42.08.2	62.33.57	0.95	...	6″
WB 529 A.....	04.02.55.2	53.15.09	16	20	3′.6
B.....	04.02.48.1	53.09.06	1.4	...	5′.2
C.....	04.02.08.8	53.12.50	1.9	...	3′.8

[a] Fluxes are primary-beam–corrected and are accurate to 5% for sources within 1′ of the field center (*IRAS* source). The rms error in the peak fluxes is 0.06 mJy beam^{-1}.

[b] Sources with no total flux listed are unresolved, and their total flux equals their peak flux.

[c] Distance between radio source and *IRAS* point source in the field (the field center).

angular distance of each source from the *IRAS* source in the center of the field. Eight of the 11 fields (73%) show emission associated with the *IRAS* source, i.e., within 45″ of the *IRAS* position, and 12 *IRAS*-associated sources are seen. The other three fields show no emission within 2′ of the *IRAS* source. From our multiple frequency observations, we conclude that 10 of these 12 sources are H II regions (see § 4.2); eight of the 10 H II regions are newly discovered.

Figures 1–5 display the maps of the five resolved or multiple *IRAS*-associated sources (S127, WB 380, 399, 436, and 440). In each figure, panel *a* is the 6 cm map (5″.5 resolution), panel *b* the 3.6 cm tapered map (5″.5 resolution), panel *c* the 2 cm map (5″.5 resolution), and panel *d* the 3.6 cm untapered map (3″ resolution). The resolutions correspond to 0.27 and 0.15 pc at a distance of 10 kpc (the typical distance for these sources). The beams for panels *a–c* are identical and are displayed in the lower right-hand corner of panel *c* in each figure; the beam for panel *d* is marked in the lower right-hand corner in each figure. The filled squares indicate the position of the *IRAS* sources, and the triangle in Figure 1 is at the position of IRAS X2127+544, a source from the *IRAS* Faint Source Catalog.

Comparison of the left-hand maps of each figure shows that the morphologies are quite similar at the three wavelengths, but most striking in S127 (see Fig. 1), though the middle map (*b*) has less extended structure than those in panel *a* or panel *c*. These similarities indicate that the emission from these regions is probably optically thin at all wavelengths, since one is seeing all the structure and therefore all the emission. This result is confirmed by the determination of the spectral indices of these sources (see § 4.2).

The more extended sources, S127, WB 399, and WB 436, all show considerably more small-scale structure in the untapered

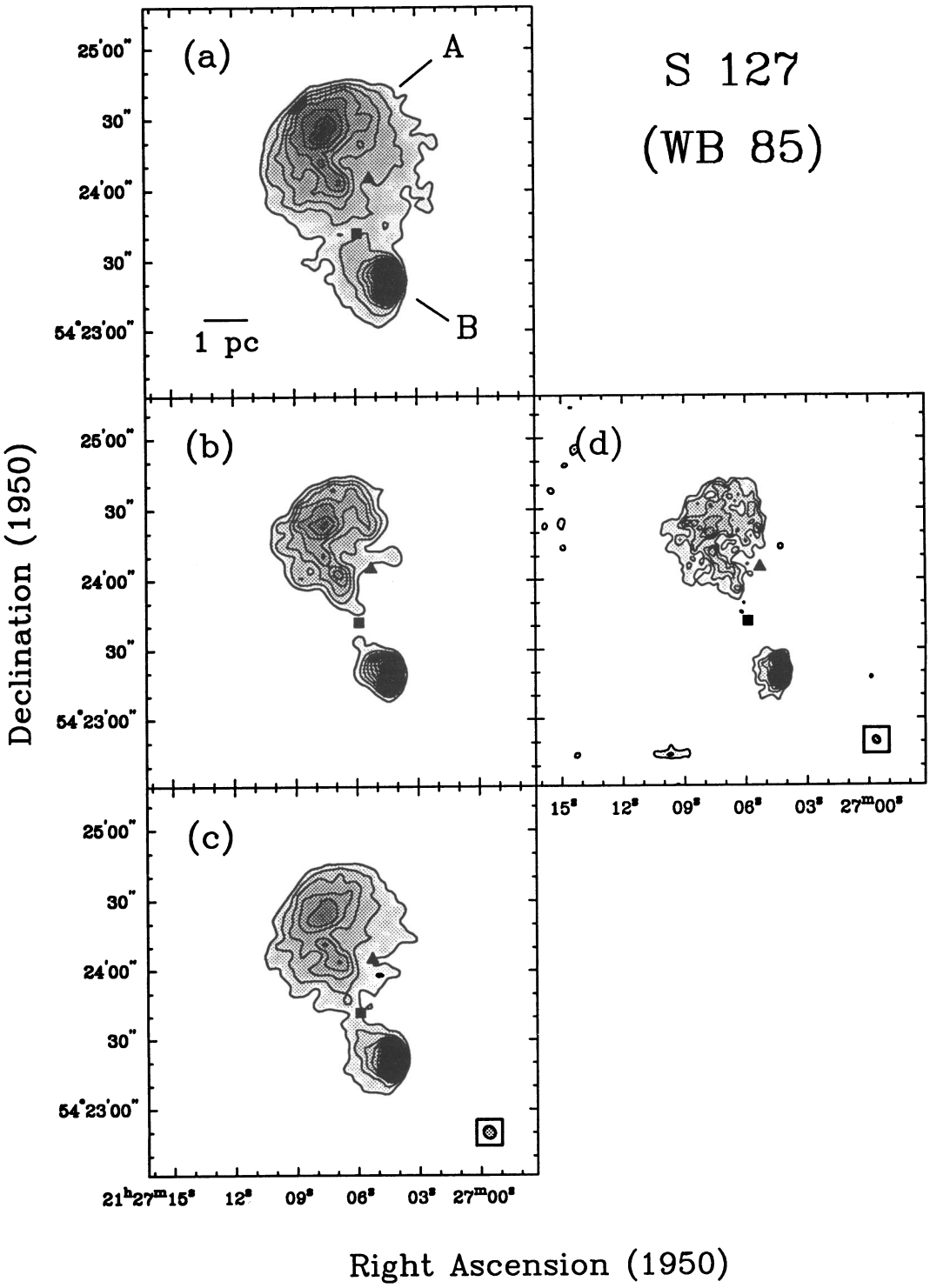

FIG. 1.—Contour maps of continuum emission from S127 (WB 85) at three wavelengths (6, 3.6, and 2 cm). The flux scale of all three wavelengths is accurate to 5%. The square represents the position of IRAS 21270+5423 and the triangle that of IRAS X2127+544. The beams for (*a*), (*b*), and (*c*) are equal (5″.5; see text) and are shown in (*c*). (*a*) 6 cm continuum emission. Contour levels are 1, 2, 3, 4, 5, 6, 7, 8, 9, 11, 13, 15, 17 × 1 mJy beam^{-1}. The rms noise in the map is 0.12 mJy beam^{-1}. (*b*) 3.6 cm continuum emission. Contour levels are the same as in (*a*). The rms noise in the map is 0.06 mJy beam^{-1}. (*c*) 2 cm continuum emission. Contour levels are the same as in (*a*). The rms noise in the map is 0.25 mJy beam^{-1}. (*d*) Untapered 3.6 cm continuum map with 3″ resolution. Contour levels are 1, 2, 3, 4, 5, 6, 7, 8, 9, 11, 13, 15, 17 × 0.5 mJy beam^{-1}. The rms noise in the map is 0.17 mJy beam^{-1}.

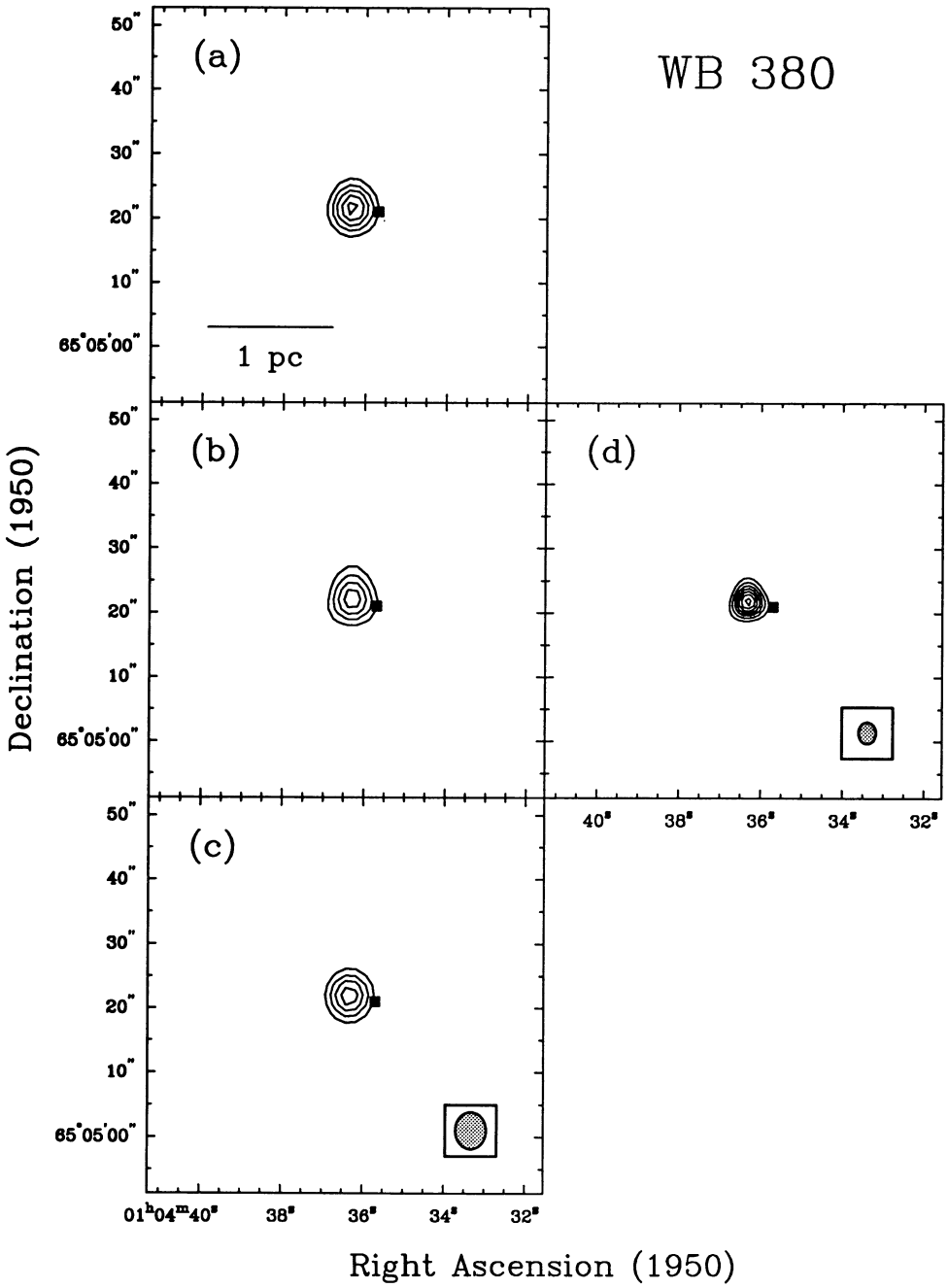

FIG. 2.—Same as Fig. 1, but for WB 380 (no gray scale). The square represents the position of IRAS 01045+6505. (*a–c*) Contour levels are 3, 5, 7, 9, 11, 13, 15 × 20 mJy beam^{-1} (1 σ = 0.18, 0.37, 0.25 mJy beam^{-1} for 6, 3.6, and 2 cm, respectively). (*d*) Contour levels are 3, 5, 7, 9, 11, 13, 15 × 10 mJy beam^{-1}.

3.6 cm maps made with the full resolution of 3″ than in the tapered 3.6 cm map, or in the 6 or 2 cm maps. In particular, S127 and WB 436 show a high degree of clumpiness down to the map resolution of 3″. Therefore, also at 6 and 2 cm, there is clearly more structure to be seen at higher resolution.

Table 4 lists the primary-beam–corrected peak and total flux density of the 10 *IRAS*-associated sources which we identify below (§ 4.2) as H II regions. At 3.6 cm are indicated the peak and total flux density for the tapered maps and, in addition, the peak flux density for the untapered maps. Table 5 lists the primary-beam–corrected peak and total flux densities of the six non–*IRAS*-associated sources which were detected at 6 and 3.6 cm and two *IRAS*-associated sources which do not have spectral indices indicative of H II region emission (note that non–

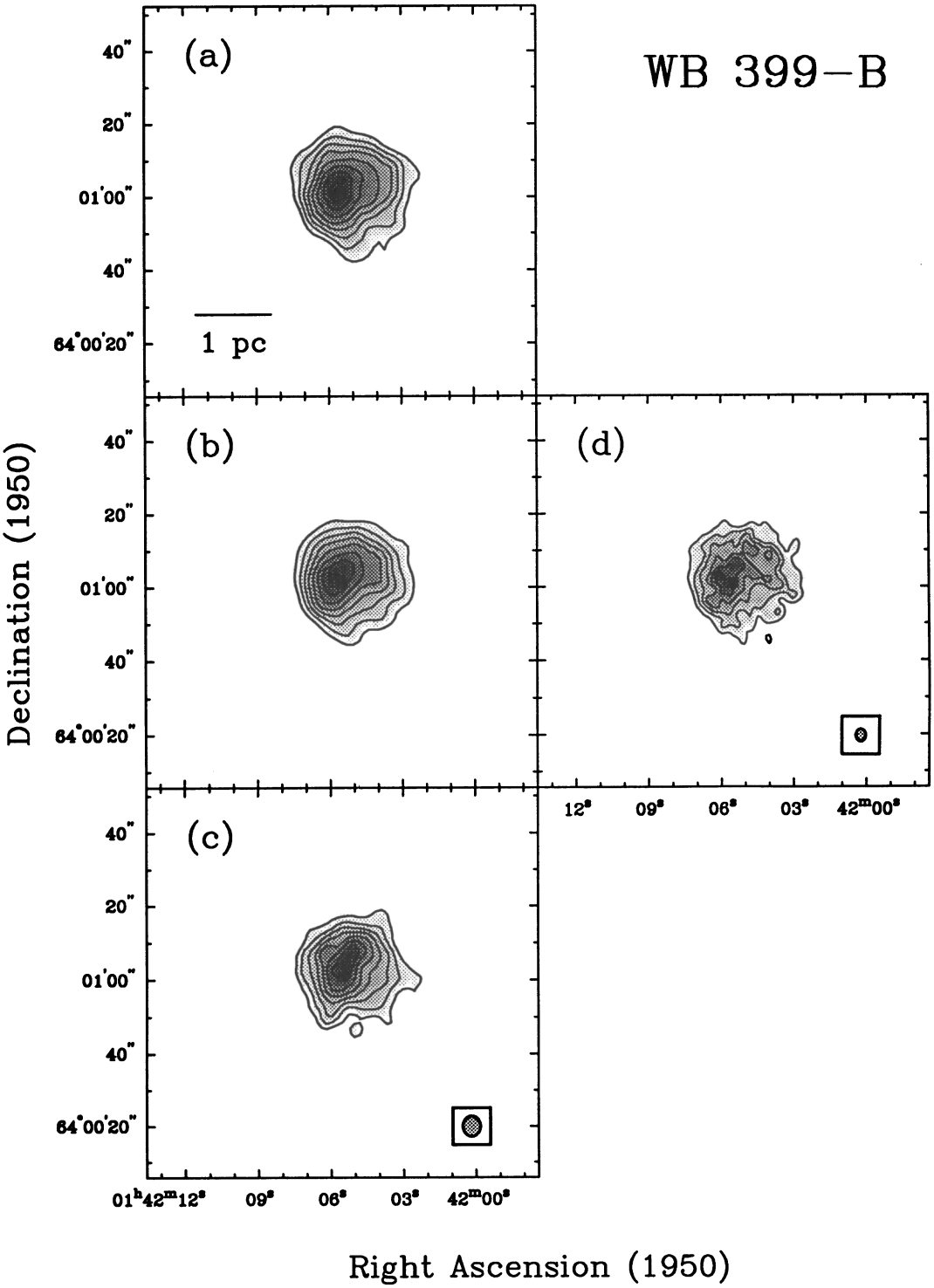

FIG. 3.—Same as Fig. 1, but for WB 399B. The square represents the position of IRAS 01420+6401. (*a–c*) Contour levels are 3, 5, 7, 9, 11, 13, 15, 17 × 0.2 mJy beam^{-1} (1 σ = 0.06, 0.05, 0.19 mJy beam^{-1} for 6, 3.6, and 2 cm, respectively). (*d*) Contour levels are 3, 5, 7, 9, 11, 13, 15, 17 × 0.1 mJy beam^{-1}. Note that the small-scale structure evident in the 2 cm map is due to noise (see § 5.3).

IRAS-associated sources in Table 3 which were only detected at 6 cm do not appear in either Table 4 or Table 5). All upper limits in flux density are 3 σ limits. The sources that were detected (denoted by three dots) for the total flux density are unresolved or barely resolved, so that the total flux density equals the peak value. The total flux densities were determined by integrating from the source center to a level for which the integrated flux density reached a maximum. For S127, which has two extended components within 60″ of each other, we integrated within nonoverlapping boxes surrounding each component. All total flux densities should be used with caution (see § 4.2).

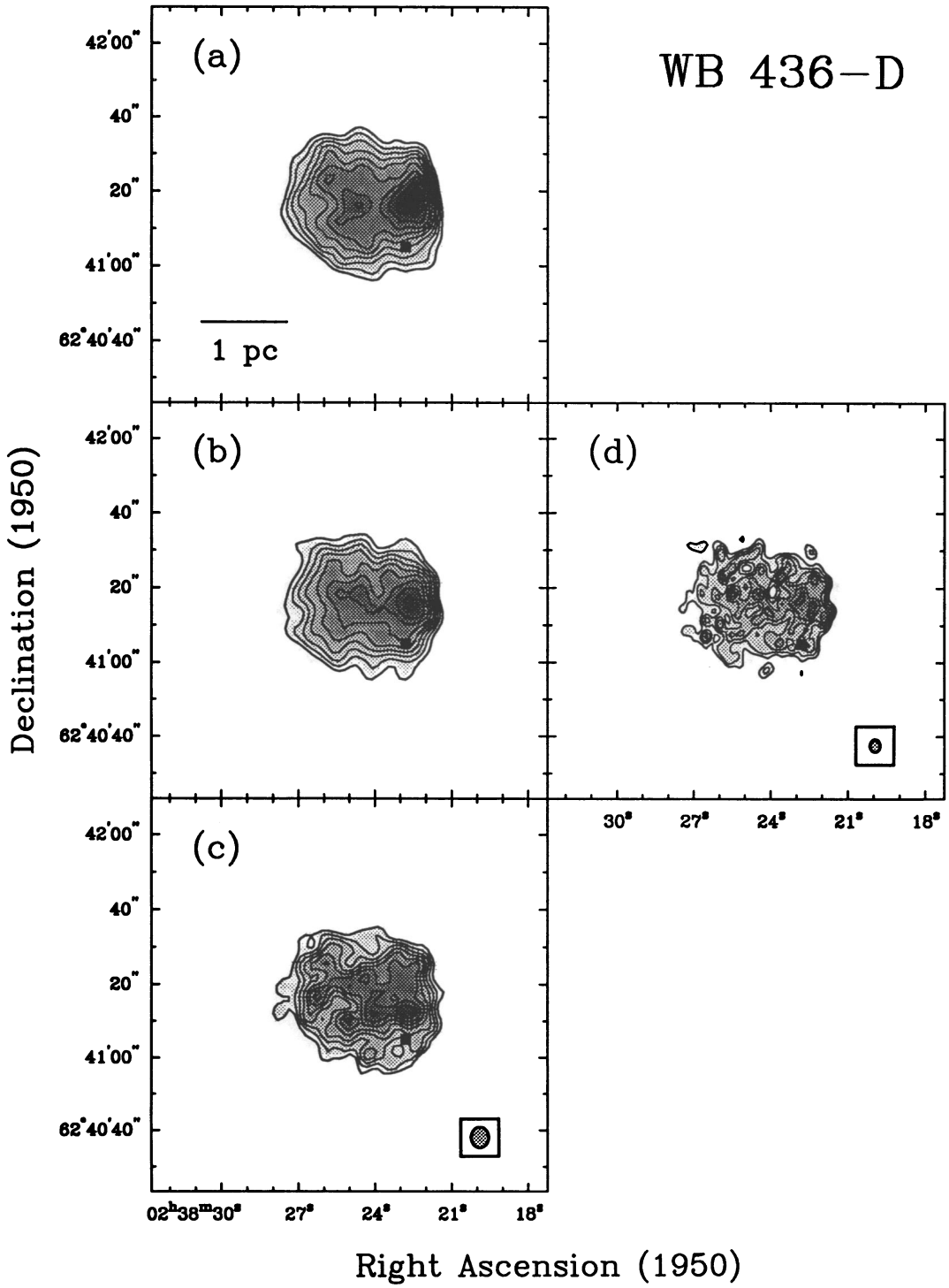

FIG. 4.—Same as Fig. 1 for WB 436D. The square represents the position of IRAS 02383+6241. (*a–c*) Contour levels are 3, 4, 5, 6, 7, 8, 9, 10, 11 × 0.2 mJy beam^{-1} (1 σ = 0.06, 0.05, 0.19 mJy beam^{-1} for 6, 3.6, and 2 cm, respectively). (*d*) Contour levels are 3, 4, 5, 6, 7, 8, 9, 10, 11 × 0.1 mJy beam^{-1}. Note that the small-scale structure evident in the 2 cm map is due to noise (see § 5.3).

4.2. *Spectral Indices and Missing Flux*

Radio continuum emission from H II regions is due to free-free emission from hot electrons. To determine whether the emission we observe is thermal, and to estimate its optical depth it is necessary to derive the spectral index by measuring the flux density at several frequencies.

Because an interferometer acts as a spatial filter, which measures certain size scales and not others, one must be careful when comparing flux densities obtained with different interferometers or even with the same interferometer at different wavelengths. The most reliable comparison can be made between the total flux density at two wavelengths, if the same fraction of flux is missing from each. This should be the case for the

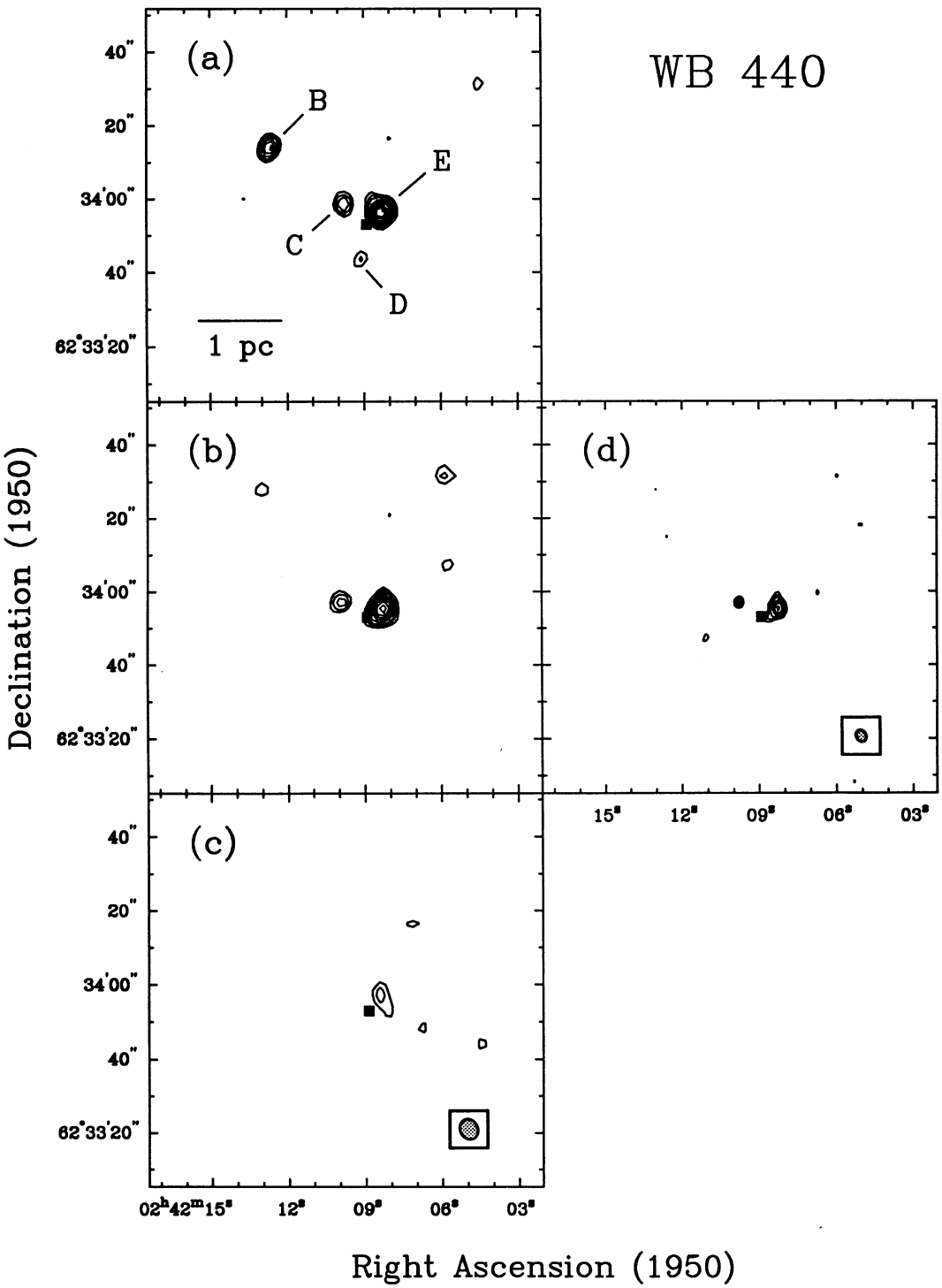

FIG. 5.—Same as Fig. 1, but for WB 440 (no gray scale). The square represents the position of IRAS 02421+6233. (*a*, *b*, *d*) Contour levels are 3, 4, 5, 7, 9, 11, 13, 15, 17 × 0.055 mJy beam^{-1} (~1 σ). (*c*) Contour levels are 3, 4 × 0.2 mJy beam^{-1} (~1 σ).

observations at 6 and 2 cm, because these were taken in "scaled arrays." Table 2 lists the largest structures that could be seen in the wavelength/configuration combinations used. For a source which is small compared to these size scales (which includes all sources except S127), the fraction of missing flux density is likely to be small, and therefore comparisons are more reliable.

To test whether we are missing a significant amount of large-scale flux, we compared the total flux density we measured at 6 cm toward the most extended source, S127, with that found in other observations. In the VLA C configuration, we obtain a total of 0.58 Jy from the two components. Fich (1993), using the VLA D configuration (which is sensitive to scales 2.5–3 times larger than the C configuration), measured 0.56 Jy;

TABLE 4

OBSERVED FLUXES FOR OUTER GALAXY H II REGIONS[a]

SOURCE	6 cm		3.6 cm	3.6 cm (T)[b]		2 cm		α(6 cm/2 cm)[c] ($\pm$0.1)
	Peak Flux (mJy beam^{-1})	Total Flux (mJy)	Peak Flux (mJy beam^{-1})	Peak Flux (mJy beam^{-1})	Total Flux (mJy)	Peak Flux (mJy beam^{-1})	Total Flux (mJy)	
WB 85A	8.39	424	2.83	7.63	203	7.03	269	−0.27
WB 85B	17.76	153	5.74	13.85	64	14.22	83	−0.30
WB 361B	0.54	...	0.46	0.52	...	0.57	...	+0.05
WB 380	234	295	158	204	284	207	262	−0.11
WB 391	0.52	0.61	0.27	0.40	0.68	<0.58	...	< −0.10
WB 399B	3.60	55.4	1.38	3.46	51.8	3.58	45.6	−0.11
WB 414C	0.18	...	0.23	0.16	...	<0.64	...	< +1.13
WB 436D	2.49	68.4	0.89	2.29	64.9	2.21	62.2	−0.06
WB 440C	0.35	...	0.30	0.31	...	<0.58	...	< +0.45
WB 440E	0.95	...	0.64	0.91	...	0.95	...	0.00

[a] Fluxes are primary-beam–corrected and are accurate to 5% at all wavelengths. The rms error in the peak fluxes is 0.06 mJy beam^{-1} at 6 cm, 0.05 mJy beam^{-1} at 3.6 cm, and 0.19 mJy beam^{-1} at 2 cm.

[b] Fluxes for maps tapered to 40 kλ to give similar resolution (5″.5) to the maps at 6 and 2 cm.

[c] Spectral index between 6 and 2 cm. The fluxes at both 6 cm and 2 cm used to calculate α are not those listed in the table but are fluxes integrated out to the 3 σ contour of the 2 cm map, so that they are integrated over the same area (see text for details). The error quoted is determined by standard propagation of error assuming that the fluxes are accurate to 5%.

Becker, White, & Edwards (1991) measured 0.54 Jy with the 3′.5 beam of the NRAO 300 foot (91 m) telescope, and Kazès, Le Squéren, & Gadéa (1975) measured a flux density of 0.6 Jy with the 1′.7 × 7′ beam of the Nançay radio telescope. Felli & Harten (1981), using the Westerbork Synthesis Radio Telescope (WSRT), observed S127 with a 6″.6 × 8″.1 beam and measured a flux density of 0.59 Jy. Thus, we clearly detected more than 95% of the total flux density from S127 and therefore expect to measure most of the emission from the other, more compact sources as well.

For such a more compact source, WB 380, we find a total 6 cm flux density of 0.295 Jy, which compares well with the 0.285 Jy found by McCutcheon et al. (1991) using the VLA in the same configuration. Becker et al. (1991) observed this source at 6 cm with the NRAO 300 foot telescope with 3′.5 resolution and found a flux density of 0.275 Jy. All three values agree within the errors, implying that we detected all the emission from this source.

An additional complication in comparing total flux densities at differing wavelengths comes about because the maps at 6 cm are ~3 times more sensitive than those at 2 cm. Thus, if the flux density is integrated above some multiple of the noise level in each map, the region covered in the 6 cm map will be larger, and the flux densities should not be compared. Therefore, in calculating the total flux density to determine the spectral index, we first created a mask at the 3 σ level in the 2 cm map and then integrated the 6 and 2 cm maps using this 2 cm mask at both wavelengths. (Note that the numbers listed in Table 4 are not these masked flux densities.) The spectral indices α between 6 and 2 cm are listed in Tables 4 (*IRAS*-associated sources with α consistent with H II region emission) and 5 (the other sources detected at multiple wavelengths). Note that since we rarely detected 2 cm emission from the latter sources, presumably due to their steep spectral indices, we calculated their spectral indices between 6 and 3.6 cm instead. The three H II region candidate sources which were not detected at 2 cm have an upper limit to the spectral index listed in Table 4.

Three of the seven sources in Table 4 with well-determined α have the theoretically expected $\alpha \approx -0.1$. With the exception of S127, which is the most extended source and therefore the

TABLE 5

MULTIFREQUENCY FLUXES FOR NON-H II REGION AND NON-*IRAS*-ASSOCIATED RADIO SOURCES[a]

SOURCE	6 cm		3.6 cm		2 cm		α(6 cm/3.6 cm)[b] ($\pm$0.1)
	Peak Flux (mJy beam^{-1})	Total Flux (mJy)	Peak Flux (mJy beam^{-1})	Total Flux (mJy)	Peak Flux (mJy beam^{-1})	Total Flux (mJy)	
WB 145A	4.6	6.0	3.3	3.7	...	...	−0.9
WB 361D	13.0	17.1	3.6	...	...	...	−2.8
WB 414A	0.51	1.06	1.05	...	...	...	−0.0
WB 414D	0.28	0.41	2.6	...	3.3	...	+1.9[b]
WB 437B	0.61	1.55	1.18	...	...	...	−0.5
WB 440B[c]	0.63	...	<0.15	...	<0.58	...	< −2.6
WB 440D[c]	0.24	...	<0.15	...	<0.58	...	< −0.9
WB 529A	16.1	19.7	10.3	14.3	...	...	−0.6

[a] Fluxes are primary-beam–corrected. The rms error in the peak fluxes is 0.06 mJy beam^{-1} at 6 cm, 0.05 mJy beam^{-1} at 3.6 cm, and 0.19 mJy beam^{-1} at 2 cm. Sources with no total flux listed are unresolved, and their total flux equals their peak flux.

[b] Spectral index between 6 and 3.6 cm, except for WB 414D, for which α is the spectral index between 6 and 2 cm. The error quoted is determined by standard propagation of error assuming that the fluxes are accurate to 5%.

[c] These two sources are within 45″ of the *IRAS* source in the field. All others are more than 2′ from the *IRAS* source.

likeliest to have differing amounts of missing flux at the two wavelengths, all sources in Table 4 have spectral indices equal to or consistent with optically thin free-free emission.

Most of the sources in Table 5 have highly negative indices, suggestive of synchrotron radiation. The two exceptions are WB 414A, which has a flat spectral index, −0.0, consistent with emission from an optically thin H II region, and WB 414D, which has a spectral index, +1.9, consistent with emission from a constant-density optically thick H II region. These two sources are 2.'9 and 1.'9 from IRAS 02071+6235, respectively, making it unclear whether they are related to the *IRAS* source. We do not consider these sources in subsequent analyses. Only two of the sources in Table 5 are within 100″ of the *IRAS* sources, WB 440B and WB 440D.

4.3. *Sizes and Morphology*

Table 6 lists the sizes and morphologies of the 10 detected H II regions and the five regions observed previously with the VLA (WBH; F93). Following the morphological designations for ultracompact H II regions by WC—spherical or unresolved (S), cometary (C), core-halo, shell, and irregular—we find that 10 out of 15 far-outer Galaxy H II regions are spherical or unresolved, and five out of 15 are cometary.

Except for S127A, S127B, and WB 436D, all the sources we detected are well fitted by an elliptical Gaussian. The sizes of these three sources were determined by measuring the extent of the 50% emission contour. Unresolved sources were taken to be smaller than the size (2″) necessary to widen the smallest beam (3″) by the positional accuracy of the maps (0.″5). Table 6 lists the measured sizes (FWHM) and the sizes obtained from a full two-dimensional Gaussian deconvolution of the beam, where we took into account the position angles of both source and beam. Each angular size θ listed in column (6) of Table 6 is the geometric mean of the two axes of the deconvolved Gaussian, which was converted to a physical diameter using the appropriate distance from Table 1. To obtain consistent sizes for the five previously observed sources, we measured the extent of the 50% contour in the maps of WBH and F93, and deconvolved these sizes using an average beam size.

4.4. *Derived* H II *Region Parameters*

Assuming that each region is an optically thin, spherical, constant-density H II region, we used the observed fluxes to determine the flux of the Lyman continuum photons required to keep the nebula ionized (N_L), the excitation parameter (U), the electron density (n_e), and the emission measure (EM). The structure in the untapered 3.6 cm maps clearly shows that both assumptions are not accurate on the smallest scales (see Figs. 1, 3, and 4), but we obtained a reasonable estimate of the average parameters. The equations used are as follows (Matsakis et al. 1976):

$$N_L = 7.5 \times 10^{43} S_\nu d^2 \nu^{0.1} T_e^{-0.45} \text{ s}^{-1} ,$$

$$U = 1.33 S_\nu^{1/3} d^{2/3} \nu^{1/30} T_e^{0.116} \text{ pc cm}^{-2} ,$$

$$n_e = 1.29 \times 10^4 S_\nu^{0.5} \nu^{0.05} d^{-0.5} \theta^{-1.5} T_e^{0.175} \text{ cm}^{-3} ,$$

$$\text{EM} = (2r) n_e^2 \text{ pc cm}^{-6} ,$$

where ν is the frequency in GHz, S_ν is the flux density measured at frequency ν in millijanskys, d is the distance to the source in kiloparsecs, θ is the angular size of the source in arcseconds, $2r$ is the diameter of the source in parsecs, and T_e is the electron temperature in units of 10^4 K.

The only undetermined parameter is the electron temperature T_e. Using radio recombination lines, Shaver et al. (1983) and Fich & Silkey (1991) found that T_e in H II regions rises with R, possibly due to the lower metallicity at large R. The value beyond $R \approx 13$ kpc is not well determined, but an extrapolation of the measurements by Fich & Silkey (1991) suggests that $T_e \approx 10^4$ K in the far-outer Galaxy. This is also the value determined for N66 and 30 Doradus in the low-metallicity Magellanic Clouds (Shaver et al. 1983). None of the

TABLE 6

OBSERVED SIZES FOR OUTER GALAXY H II REGIONS

SOURCE (1)	MORPHOLOGY (2)	d (kpc) (3)	SIZE (arcsec) Measured[a] (4)	SIZE (arcsec) Deconvolved[b] (5)	θ (arcsec) (6)	$2r$ (pc) (7)	REFERENCE (8)
WB 85A	C	11.5	37 × 25	37 × 24	30	1.7	1
WB 85B	C	11.5	14 × 8	13 × 6.5	9	0.5	1
WB 361B	S	12.2	Unresolved	<2	<2	<0.12	1
WB 380	S	10.7	6.3 × 5.5	2.6 × 2.7	2.6[c]	0.13	1
WB 391	S	10.5	7.1 × 5.1	4.3 × 2	2.9	0.15	1
WB 399B	S	10.1	21.5 × 20.5	21 × 20	20	1.0	1
WB 414C	S	9.9	Unresolved	<2	<2	<0.10	1
WB 436D	C	9.0	35 × 23	35 × 23	28	1.2	1
WB 440C	S	9.3	6.6 × 5.0	3.8 × <2	<2.8	<0.12	1
WB 440E	S	9.3	6.0 × 5.5	2.9 × 2	2.4	0.11	1
WB 770	C	7.6	77 × 55	76 × 53	63	2.3	2
WB 794	C	9.4	39 × 34	36 × 31	33	1.5	2
WB 852	S	6.9	28 × 24	23 × 17	20	0.7	3
WB 952	S	7.2	32 × 28	29 × 24	26	0.9	2
WB 1006	S	8.1	Unresolved	<5	<5	<0.20	3

[a] The sizes from this work are accurate to approximately ±0.″5. The sizes from other works have been measured from the 50% contours of the maps, to be consistent with this work.

[b] The resolution of the F93 maps is ∼14″, and the resolution of the WBH maps is ∼16.″5.

[c] This size exactly matches that found with the same configuration of the VLA by McCutcheon et al. 1991, who mistakenly categorized this source as a "well-developed H II region."

REFERENCES.—(1) This work. (2) F93. (3) WBH.

TABLE 7

DERIVED PARAMETERS OF OUTER GALAXY H II REGIONS[a]

Source	(n_e^{peak})[b] (cm^{-3})	$\langle n_e \rangle$[c] (cm^{-3})	EM (pc cm^{-6})	U (pc cm^{-2})	log N_L (s^{-1})	ZAMS
WB 85A	1.4×10^3	5.1×10^2	4.5×10^5	53.6	48.69	O7
WB 85B	...	1.9×10^3	1.8×10^6	38.2	48.25	O8.5
WB 361B	...	$>1.0 \times 10^3$	$>1.2 \times 10^5$	6.1	45.85	B0.5
WB 380	...	1.7×10^4	3.8×10^7	45.3	48.47	O7.5
WB 391	...	6.8×10^2	6.9×10^4	5.7	45.77	B0.5
WB 399B	1.0×10^3	3.6×10^2	1.3×10^5	25.0	47.70	O9.5
WB 414C	...	$>6.7 \times 10^2$	$>4.5 \times 10^4$	3.6	45.19	B1
WB 436D	8.6×10^2	2.6×10^2	8.1×10^4	24.8	47.69	O9.5
WB 440C	...	$>5.8 \times 10^2$	$>4.0 \times 10^4$	4.4	45.42	B1
WB 440E	...	1.2×10^3	1.6×10^5	6.1	45.86	B0.5
WB 770	...	1.1×10^2	2.8×10^4	26.3	47.76	O9.5
WB 794	...	2.2×10^2	7.3×10^4	28.2	47.86	O9.5
WB 852	...	2.5×10^2	4.4×10^4	14.6	47.00	B0
WB 952	...	9.3×10^2	7.8×10^5	44.0	48.43	O7.5
WB 1006	...	$>1.3 \times 10^3$	$>3.4 \times 10^5$	11.9	46.73	B0.5

[a] Values for sources above the space break are derived from data in this work. Values for sources below the space break are derived from the sizes in Table 6 and from the fluxes given in the references in Table 6.

[b] Peak electron density calculated for sources in this work which are well resolved in the highest resolution maps (3″).

[c] Average electron density calculated from the total 6 cm flux and the size of the source.

derived parameters is very sensitive to T_e, and we use $T_e = 10^4$ K for all our calculations.

Table 7 lists the derived parameters for the 10 detected H II regions and the five previously detected H II regions. For the regions (S127, WB 399, and WB 436) which are well resolved in the highest resolution maps, we determined the peak electron density (n_e^{peak}) in an unresolved clump using the peak 3.6 cm flux density and taking the size of the clump to be the beam size (3″). From the total flux densities and the sizes of the sources from Table 6, we determined the average electron density ($\langle n_e \rangle$); for unresolved sources, this number is a lower limit. In the last column of Table 7 is listed the spectral type of the single ZAMS star which could provide a flux of ionizing photons equal to N_L (Panagia 1973). These spectral types fall in the range B1–O7, in agreement with the FIR luminosity selection criterion, $L_{FIR} \gtrsim 10^4\ L_\odot$. However, a cluster of many later type stars could also provide the necessary ionization (see § 5.4).

5. DISCUSSION

5.1. *Sizes and Lifetimes*

Habing & Israel (1979) categorized H II regions by their sizes, electron densities, and emission measures. They define ultracompact H II regions as those with $n_e \gtrsim 3000$ cm^{-3}, $d \lesssim 0.15$ pc, and EM $> 10^6$ pc cm^{-6}, and compact H II regions as those with $n_e \gtrsim 1000$ cm^{-3}, $d = 0.1$–1.0 pc, and EM $> 10^5$ pc cm^{-6}. In Tables 6 and 7, $d = 2r$ ranges from less than 0.10 pc to 2.3 pc, n_e ranges from 100 to $\gtrsim 1.7 \times 10^4$ cm^{-3}, and EM ranges from 2.8×10^4 to 3.8×10^7 pc cm^{-6}. Therefore, many of our sources are compact or ultracompact H II regions. Because our sample is drawn from the *IRAS* Point-Source Catalog, we expect to select mainly (ultra)compact H II regions. However, our observations are sensitive to structures as large as 4 pc (at a distance of 10 kpc), and the absence of such large sources is striking.

Wood & Churchwell (1989; WC), following Dyson & Williams (1980), discuss a simple model of the expected evolution of an H II region embedded in a homogeneous molecular cloud. Such an H II region expands quickly (within a few years) to its initial Strömgren radius ($r_i = 0.02$–0.05 pc) for typical H II region and molecular cloud parameters. Then the hot, high-pressure, ionized gas expands until it reaches pressure equilibrium with the surrounding cloud.

If the measured sizes reflect this evolution, then one would expect that the fraction of H II regions of a given size would be proportional to the length of time an H II region spends at that size. We observed all 11 sources in our sample in the range $l = 85°$–$150°$ and $R \gtrsim 15$ kpc, and of these, more than half (six) are smaller than 0.15 pc. According to this simple model, such sizes correspond to H II region ages of $\lesssim (3$–$5) \times 10^4$ yr, $\sim 1\%$ of the main-sequence lifetime of an O7–B0 star with mass loss (Maeder & Meynet 1987). This small percentage is in contrast with the 10% or 20% of O stars in the ultracompact H II regions phase deduced by WC and Codella & Palla (1995), respectively, suggesting that the assumption that the sizes of H II regions reflect their ages in such a simple way does not hold. WC, in their study of ultracompact H II regions, found a similar result and suggest three possible mechanisms to keep H II regions from expanding freely. The first is that infall onto the H II region impedes the expansion of the ionization front. The second mechanism is that cometary H II regions are formed when an O star (possibly with a wind) moves supersonically through the surrounding molecular cloud, forming a bow shock on the side of the direction in which the star is moving. A third possibility is that compact H II regions are formed when the strong stellar wind from the newly formed O star photoevaporates its accretion disk, forming an ionized disk wind that can persist for up to 10^5 yr (Hollenbach, Johnstone, & Shu 1993).

Although the sizes of the H II regions clearly do not reflect their absolute ages, their relative sizes might be indicative of age differences. Some support for the latter comes from a comparison of our continuum maps with molecular line maps of S127 and WB 380. S127 is an optical H II region, in contrast to the optically invisible WB 380. De Geus et al. (1996) have observed these two sources in CO ($J = 1 \rightarrow 0$) with the

Berkeley-Illinois-Maryland Array (BIMA) millimeter interferometer, and in CS ($J = 2 \rightarrow 1$) with both the interferometer and the IRAM 30 m telescope. S127, which contains two radio H II regions with sizes of 0.5 and 1.7 pc (see Table 6), shows considerable CO emission but little CS emission, which traces dense ($n \gtrsim 10^5$ cm^{-3}) molecular gas, whereas WB 380 contains an ultracompact H II region centered on a bright compact CS clump. These results suggest an evolutionary scenario, where there has been enough time for the two larger H II regions to disrupt the dense cores from which the exciting O stars had formed, but where the ultracompact H II region is too young to have affected its surroundings.

WB 436 and WB 437 may provide another example of an evolutionary sequence of star formation. The kinematic distances of the two sources are almost equal, and their projected separation is only 23.5 pc. The low-resolution CO ($J = 1 \rightarrow 0$) map of Brand & Wouterloot (1994) shows that both objects are associated with the same molecular cloud, yet WB 436 is an optically visible nebula and shows radio emission indicating the presence of high-mass star formation, while WB 437 shows no nebulosity or radio emission, in spite of the presence of a strong *IRAS* point source. Evidence for star formation near WB 437 is provided by the IRAM observations of CO ($J = 2 \rightarrow 1$) emission from WB 437, which show strong wings in a very small ($\lesssim$0.5 pc) region, indicating the presence of an outflow source (Wouterloot & Brand 1996), and by the near-infrared detection of a cluster of stars centered at the *IRAS* position (Lada & de Geus 1996). The lack of optical nebulosity and radio continuum emission from WB 437 suggests that the young stellar objects near WB 437 are still embedded (see § 5.4), and that star formation is at an earlier stage than in WB 436.

5.2. *Morphological Classification*

Wood & Churchwell (1989; WC) classified the morphology of ultracompact H II regions into five types with the following distribution: spherical or unresolved (43%), cometary (20%), core-halo (16%), shell (4%), and irregular or multiply peaked (17%). In our small sample, we find five cometary H II regions and 10 sources which are spherical or unresolved, roughly consistent with WC. Our survey has much lower resolution than the WC survey (3″ versus 0.″4), and higher resolution observations of the unresolved or barely resolved sources will probably reveal at least some of them to have structure. Therefore, the number of cometary regions (five out of 15) should be treated as a lower limit.

Cometary H II regions have been explained in several ways. One of the earliest explanations was the "blister" (Israel 1978) or "champagne flow" (Tenorio-Tagle 1979; Yorke, Tenorio-Tagle, & Bodenheimer 1983) model, in which an H II region forms on the edge of a molecular cloud and expands freely into the intercloud medium, while the pressure from the cloud confines the H II region on the other side, forming the cometary shape. Two of the cometary H II regions we detected are associated with the optical H II region S127. The molecular cloud associated with S127 has been completely mapped in CO at low resolution (60″) with the Kitt Peak 12 m telescope, and the area immediately around the H II region was studied at high resolution (6″–7″) with the BIMA millimeter interferometer (de Geus et al. 1996). The large-scale maps show that the H II regions are located near the northwest edge of the molecular cloud, and the high-resolution maps show that there is molecular gas associated with the two cometary H II regions. In particular, there is a ridge of molecular material to the west of S127B at the correct position to provide confinement of the H II region.

5.3. *Optically Thick Clumps*

The 2 cm maps of WB 399 and WB 436 seem to differ slightly from the 6 and 3.6 cm maps taken at the same resolution (see Figs. 3 and 4). The large-scale emission from these regions is coming from optically thin free-free emission (see Table 4 and § 4.2), but the small-scale differences might be explained by the presence of small optically thick clumps, whose flux densities are rising with frequency, embedded in an optically thin halo of gas. At lower frequencies, these clumps would emit no significant emission, but at higher frequencies they would "pop up" above the optically thin emission, which is falling slowly with frequency. To test this hypothesis, we scaled the 6 cm maps of these two sources between 5 and 15 GHz by $\nu^{-0.1}$ and then subtracted them from the 2 cm maps. Figures 6 and 7 show the 6 cm, 2 cm, and difference maps for WB 399 and 436, respectively. The contours in the difference maps are ± 2, ± 3, and ± 4 times the rms noise levels. Although there is a 4 σ peak in the WB 399 difference map, there are two -4 σ peaks as well. For WB 436 the difference map shows only ± 3 σ peaks. Thus, in spite of the seemingly striking difference between the 6 and 2 cm map morphologies, from our data it is not possible to conclude that there are optically thick clumps in these H II regions.

5.4. *Comparison of Radio and FIR Data*

Because of our selection criterion, $L_{\rm FIR} \gtrsim 10^4\ L_\odot$, all of these sources have considerable FIR radiation associated with them. This FIR emission is usually interpreted as thermal emission by dust in the H II region itself or in the surrounding molecular cloud, which has been heated by stellar radiation. Thus, the total luminosity from a source, $L_{\rm FIR}$ (see Table 1), is a measure of the luminosity of all the stars within the *IRAS* beam. In § 4.4, we calculated the flux of the Lyman continuum photons ($N_{\rm L}$) necessary to keep each nebula ionized (see Table 7). A comparison between $L_{\rm FIR}$ and $N_{\rm L}$ can indicate whether the ionizing flux exciting the H II region is coming from a single star or from more than one star. Figure 8 shows a plot of log $N_{\rm L}$ versus log $L_{\rm FIR}$ for the 15 sources detected in this study or by WBH or F93 (the sources WB 770 = S259 and WB 794 = S266 are plotted without their very large error bars, caused by large distance errors). The error in log $L_{\rm FIR}$ was determined from the error in the kinematic distance, assuming an uncertainty of 6.6 km s^{-1} in the $V_{\rm lsr}$ of the sources (the velocity dispersion of local molecular clouds [Stark 1984]; see also Stark & Brand 1989), and the error in log $N_{\rm L}$ was determined from a combination of the distance error and the 5% error in the flux densities. The nondetections are plotted as upper limits in log $N_{\rm L}$. Since the *IRAS* beam collects emission from a much larger area, it is impossible to divide the flux density between multiple sources in one region. Thus, for S127 and WB 440, the total $N_{\rm L}$ from all H II regions has been used.

The solid line in Figure 8 connects the squares, which represent single ZAMS stars calculated from model atmospheres (Panagia 1973). The dotted line in Figure 8 connects the triangles, which represent clusters of stars, and are labeled with the spectral type of the most massive cluster member. To calculate the positions of clusters of stars in this plot, we have to adopt a cluster mass function. Although there is evidence that the initial mass function (IMF) of massive stars ($M \gtrsim 10 - 20$

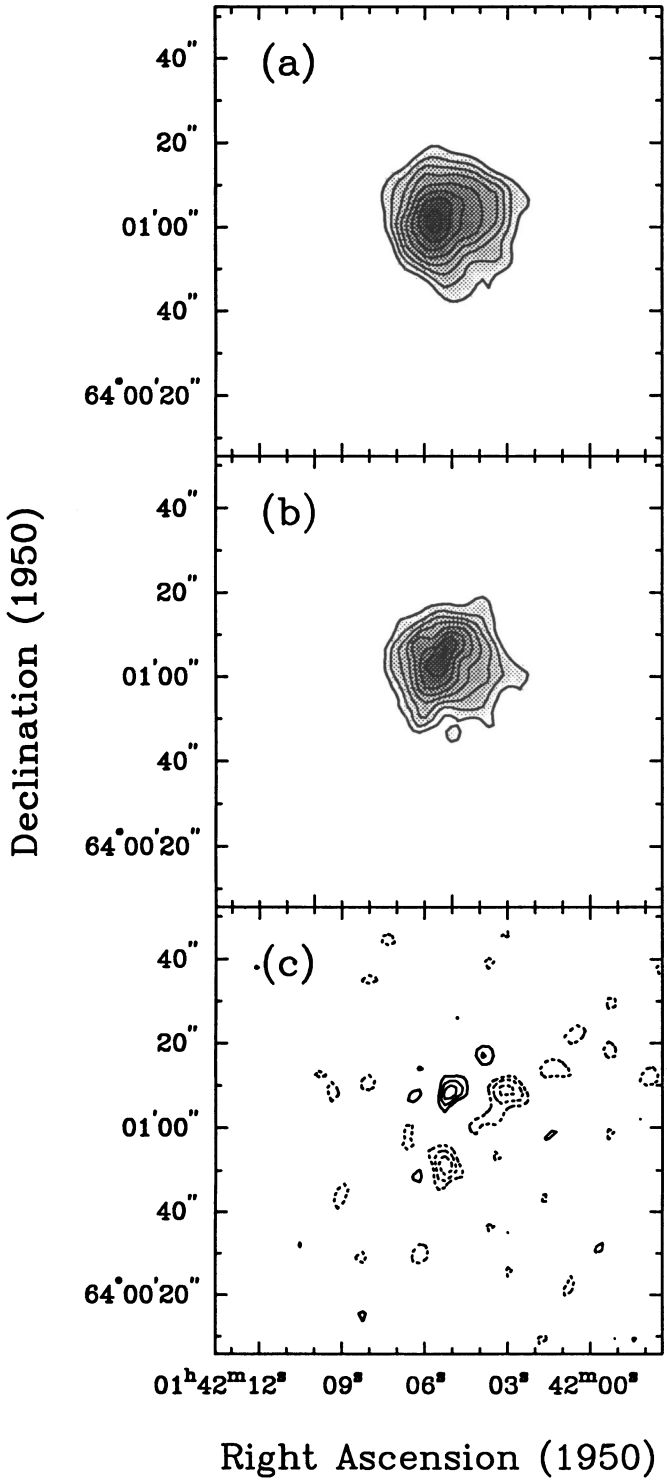

FIG. 6.—(*a*) Contour map of 6 cm continuum emission from WB 399, with gray scale overlaid. Contour levels are 3, 5, 7, 9, 11, 13, 15, 17 × 0.2 mJy beam^{-1}. (*b*) Contour map of 2 cm continuum emission from WB 399, with gray scale overlaid. Contour levels are 3, 5, 7, 9, 11, 13, 15, 17 × 0.2 mJy beam^{-1}. (*c*) Difference of 2 cm map and 6 cm map scaled from 5 to 15 GHz by $\nu^{-0.1}$. Contour levels are −4, −3, −2, 2, 3, 4 × 0.2 mJy beam^{-1} (∼1 σ).

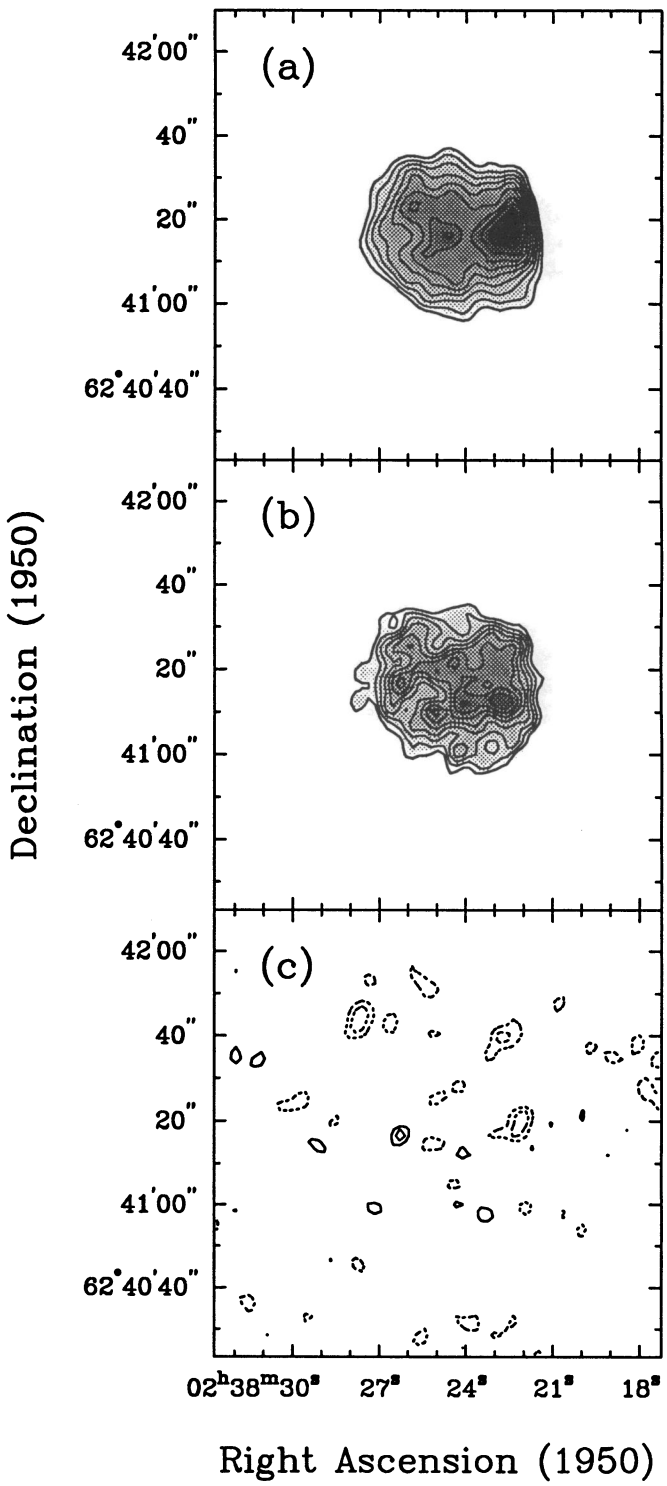

FIG. 7.—(*a*) Contour map of 6 cm continuum emission from WB 436, with gray scale overlaid. Contour levels are 3, 4, 5, 6, 7, 8, 9, 10, 11 × 0.2 mJy beam^{-1}. (*b*) Contour map of 2 cm continuum emission from WB 399, with gray scale overlaid. Contour levels are 3, 4, 5, 6, 7, 8, 9, 10, 11 × 0.2 mJy beam^{-1}. (*c*) Difference of 2 cm map and 6 cm map scaled from 5 to 15 GHz by $\nu^{-0.1}$. Contour levels are −3, −2, 2, 3 × 0.2 mJy beam^{-1} (∼1 σ).

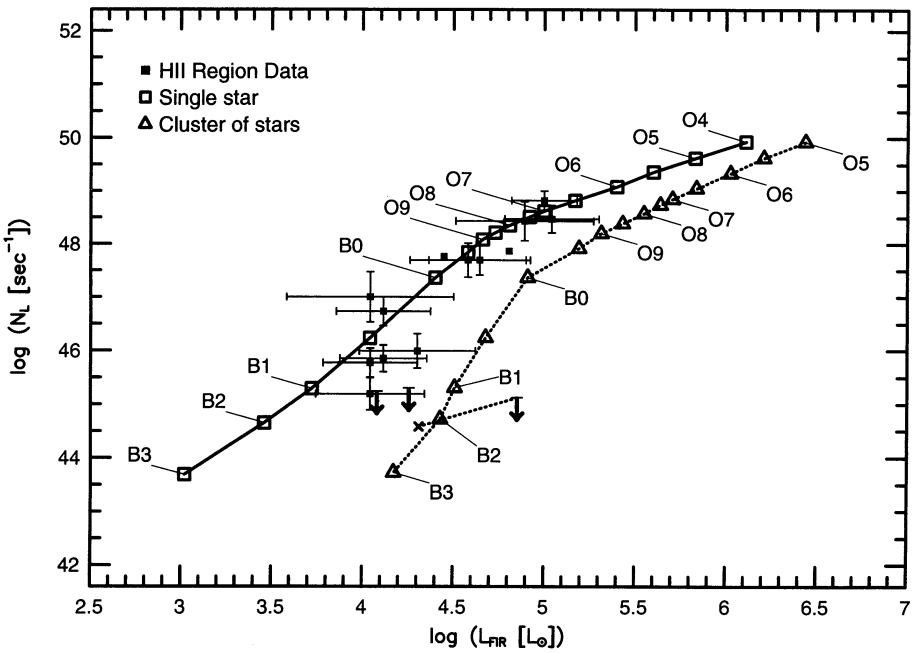

FIG. 8.—Plot of log N_L vs. log L_{FIR} for the 15 regions observed to date in this study (the regions S259 [WB 770] and S266 [WB 794] are plotted without their large error bars, caused by large distance errors). The solid line connects the squares which plot the ionizing flux and total luminosity from a ZAMS star of the spectral type indicated. The dotted line connects the triangles which plot the same quantities for a Miller-Scalo IMF cluster with the spectral type of the most massive cluster member indicated. See text (§ 5.4) for additional discussion of the figure.

$M_\odot$) differs between the inner and outer Galaxy (Garmany, Conti, & Chiosi 1982; Wouterloot et al. 1995), observations of the IMF of star clusters, including both massive and intermediate-mass stars, show no evidence for a variation of the IMF with R (Tarrab 1982; Sagar et al. 1986). In addition, the IMFs of clusters and field stars do not differ significantly (Scalo 1986). Thus, we have chosen to use the well-known IMF of Scalo (1986, similar to that of Miller & Scalo 1979). We emphasize that we are not attempting to determine the IMF in the outer Galaxy but merely want to demonstrate the effect of a cluster of stars on positions of points in Figure 8.

For each cluster, we chose the spectral type of the most massive star and derived the cluster membership using the adopted IMF. The cluster luminosity and the number of Lyman continuum photons were then calculated using the results of Panagia (1973), relating mass to spectral type using Mihalas & Binney (1981). The lower mass cutoff was taken to be 0.1 $M_\odot$, an M6 star.

N_L is a much steeper function of spectral type than is the stellar luminosity, so the result of adding a Miller-Scalo cluster to the most massive cluster member is to add, besides a small amount of ionizing flux, relatively more luminosity. This effect is more pronounced the earlier the spectral type of the most massive cluster member. The point for an O8 star is shifted up by roughly a factor of 1.7 in N_L but is shifted to the right by a factor of 5.5 in luminosity (see Fig. 8). Another factor which will affect the location of a point in Figure 8 is the amount of dust in the H II region. Dust in an H II region can absorb some of the UV flux from the star before it is able to ionize any gas, thereby reducing N_L. WC showed that in their sample of ultracompact H II regions, 50%–90% of the UV photons emitted by the newly formed star must be absorbed by dust *within* the H II region. Kurtz et al. (1994) concluded that at least half their sources must be excited by a stellar cluster, and that almost all of their sources must contain some dust. Comparison of the data points with the curves in Figure 8 shows that, with the exception of WB 437, the flux densities from most sources with $L \gtrsim 3 \times 10^4\ L_\odot$ are consistent with a single star exciting a dust-free H II region, whereas the less luminous sources have a range of ionizing fluxes which makes their interpretation less clear. Because metal abundances probably are much lower at large R (see, e.g., Shaver et al. 1983; Wilson & Matteucci 1992; Wouterloot & Brand 1996; Rudolph et al. 1996), the influence of dust might be less than in H II regions in the solar neighborhood or in the inner Galaxy.

The source WB 437 is somewhat intriguing. The FIR luminosity suggests the presence of an O8 star, but the upper limit to the radio flux density ($\log N_L < 45.12$) indicates that the earliest spectral type allowed is B1. The radio and FIR flux densities cannot be reconciled even with a Miller-Scalo IMF cluster (see Fig. 8). One possibility for this discrepancy is that the source contains an extremely large cluster of stars with spectral type later than B1, large enough to provide a luminosity of $7 \times 10^4\ L_\odot$. Near-infrared observations with the Kitt Peak 4 m telescope (Lada & de Geus 1996) have revealed the existence of a cluster of stars embedded in this cloud; it is still unclear whether this cluster could provide the necessary luminosity. It is possible, however, to explain the WB 437 data if, in contrast to most of the other far-outer Galaxy sources, most ($\sim$90%) of the UV radiation of the cluster is absorbed by dust (this would have the effect of moving the star and cluster curves down in Fig. 8). Kurtz et al. (1994) also see evidence for sources best explained by such large amounts of dust absorption.

If WB 437 contains an extremely young H II region, which is still optically thick at 15 GHz, it could also be undetectable at that frequency. If a single O8 star is exciting this H II region, then the 2 cm flux density of less than 0.58 mJy implies that the H II region must have a radius less than 700 AU = 1.1×10^{16} cm, an electron density greater than 1.3×10^6 cm^{-3}, and an emission measure greater than 1.1×10^{10} pc cm^{-6}, all rather

extreme. The spectrum of this H II region would only turn over above 50 GHz, and it would have a flux density at 100 GHz of 0.23 Jy, which should be easily detectable.

An alternative to a young cluster or a very compact, optically thick H II region is that the FIR luminosity comes from the gravitational energy of infall. There is no direct evidence for this speculation, although strong CO wings have been found (Wouterloot & Brand 1996), which usually, however, are attributed to outflow. The lack of radio continuum from this luminous FIR source merits further investigations into the kinematics of the molecular gas in this cloud, to look for indications of collapse.

One last possibility is that the kinematic distance of WB 437 has been overestimated. Note that in this case the distance of WB 436, which is associated with the same molecular complex (Brand & Wouterloot 1994), would also change. Brand & Blitz (1993) find that the residuals of observed radial velocities of H II regions and reflection nebulae minus the velocity predicted by their fitted rotation curve are between 0 and -25 km s^{-1} at the Galactic longitude of WB 437. Using the most extreme residual, -25 km s^{-1} would imply that the distance to WB 437 is 4.9 kpc, and the data point would move to the location marked with a cross in Figure 8. Such an extreme distance error would make the FIR and Lyman continuum luminosities consistent with a cluster of the earliest spectral type of B2. In any case, the strong FIR emission and the lack of radio continuum emission indicate that this region is undergoing star formation, and that the region is very young.

One of the most luminous *IRAS* sources, associated with S127, actually consists of two distinct H II regions, even though its position on the plot implies that a single star could provide both the total luminosity and the ionizing flux. This apparent contradiction occurs because N_L is dominated by the brighter of the two radio sources, whereas the luminosities implied from the ionizing fluxes differ by only a factor of 2. Thus, within the errors in both N_L and L_{FIR} (dominated by the distance errors), these two H II regions are consistent with a single star providing the excitation and the luminosity for each source.

6. SUMMARY

We have made a systematic, multifrequency radio continuum survey of some of the most luminous and distant *IRAS* sources in the catalog of Wouterloot & Brand (1989; WB 89). We selected the 31 sources with well-determined Galactocentric distances, $R \gtrsim 15$ kpc, and with $L_{FIR} \gtrsim 10^4$ $L_\odot$ to search for H II regions at the outer edge of the Galactic disk. We used the VLA to resolve small-scale structure and to be able to compare our maps with high-resolution molecular line maps we made of some of these sources (de Geus et al. 1996).

We observed 11 fields at 6, 3.6, and 2 cm; eight showed emission associated with the *IRAS* source, and we found a total of 12 associated sources. Of these 12, 10 were found to have spectral indices consistent with optically thin, free-free emission, indicating that they are H II regions. Eight of these 10 H II regions (which have $R = 15.0$–18.2 kpc) have been newly discovered, indicating that WB89's selection criteria are very successful at identifying active sites of star formation in the outer Galaxy. Together with earlier VLA observations which fit our selection criteria, a total 15 H II regions have been identified in the far-outer Galaxy using the WB89 catalog.

We used the measured flux densities and sizes to determine the electron densities, emission measures, and excitation parameters of the H II regions, and the fluxes of Lyman continuum photons, N_L, needed to keep the nebulae ionized. Of the 15 H II regions, seven have sizes $\lesssim 0.20$ pc. Assuming a simple model of pressure-driven expansion of the ionized gas into the surrounding ISM predicts that these regions have lifetimes $\lesssim 5 \times 10^4$ yr, less than 1% of the lifetime of an O star, suggesting that these compact H II regions have much larger lifetimes than inferred by this simple model.

Comparison of the radio continuum maps with CO ($J = 1 \rightarrow 0$) and CS ($J = 2 \rightarrow 1$) maps of S127 and WB 380 reveals that the more compact H II region in WB 380 (size 0.13 pc) is still embedded in a dense CS-emitting core, while the more extended H II regions in S127 (sizes 0.5 and 1.7 pc) show little CS emission. This suggests that the H II regions in S127 are older than the one in WB 380 and have had time to clear away the dense core from which they formed, while the younger, ultracompact H II region has not had as much time to affect its surroundings.

A large fraction (five out of 15) of the H II regions have cometary shapes; the rest are spherical or unresolved. Comparison of our continuum map of S127 with the high-resolution BIMA millimeter interferometer map of de Geus et al. (1995) shows that the cometary structure of the two H II regions could be due to pressure confinement in one direction by the surrounding molecular cloud (the "blister" or "champagne flow" model).

Comparison of our radio continuum data with the *IRAS* FIR flux densities (specifically N_L and L_{FIR}) shows that the excitation of the five most luminous H II regions we observed can be explained as being due to a single O or B star exciting a dust-free H II region. This is in contrast to results for inner Galaxy sources (WC; Kurtz et al. 1994). The high-luminosity source WB 437 shows no radio continuum emission, which could be due to a variety of reasons. Possibilities we suggest are that more than 90% of the ionizing radiation could be absorbed by dust in the H II region; that the region may contain a large cluster of low-mass nonionizing stars; that the region contains a very compact, optically thick H II region; that part of the luminosity arises from the gravitational energy of infall; or that a large error is made in the distance estimate due to a large deviation from circular motion.

A. L. R. wishes to acknowledge the support of a National Research Council Fellowship while at NASA/Ames Research Center, and of a New Faculty Research Grant at Harvey Mudd College. We wish to acknowledge the support of NATO Collaborative Research Grant 920835, which facilitated the travel necessary to complete this work. E. dG. acknowledges partial support by funds from the Margaret Cullinan Wray Charitable Lead Annuity Trust, and NSF grant AST-8918912 to the University of Maryland.

REFERENCES

Becker, R. H., White, R. L., & Edwards, A. L. 1991, ApJS, 75, 1
Bloemen, J. B. G. M., Deul, E. R., & Thaddeus, P. 1990, A&A, 233, 437
Brand, J., & Blitz, L. 1993, A&A, 275, 67
Brand, J., Blitz, L., & Wonterloot, J. G. A. 1986, A&AS, 65, 537
Brand, J., & Wouterloot, J. G. A. 1994, A&AS, 103, 503
———. 1995, A&A, in press
Carpenter, J. M., Snell, R. L., & Schloerb, F. P. 1990, ApJ, 362, 147
Caswell, J. L., & Haynes, R. F. 1987, A&A, 171, 261
Codella, C., & Palla, F. 1995, A&A, in press
de Geus, E. J., Brand, J., Rudolph, A. L., & Wouterloot, J. G. A. 1996, in preparation
Dyson, J. E., & Williams, D. A. 1980, Physics of the Interstellar Medium (New York: Wiley)
Felli, M., & Harten, R. H. 1981, A&A, 100, 28
Fich, M. 1986, AJ, 92, 787
———. 1993, ApJS, 86, 475 (F93)
Fich, M., & Silkey, M. 1991, ApJ, 366, 107
Garmany, C. D., Conti, P. S., & Chiosi, C. 1982, ApJ, 263, 777
Habing, H. J., & Israel, F. P. 1979, ARA&A, 17, 345
Hollenbach, D., Johnstone, D., & Shu, F. 1993, in Massive Stars: Their Lives in the Interstellar Medium, ed. J. P. Cassinelli & E. B. Churchwell (San Francisco: ASP), 26
Israel, F. P. 1978, A&A, 70, 769
Kallas, E., & Reich, W. 1980, A&AS, 42, 227 (KR)
Kažes, I., Le Squéren, & Gadéa, F. 1975, A&A, 42, 9
Kerr, F. J., & Lynden-Bell, D. 1986, MNRAS, 221, 1023
Kurtz, S., Churchwell, E., & Wood, D. O. S. 1994, ApJS, 91, 659
Lada, E., & de Geus, E. J. 1996, in preparation
Maeder, A., & Meynet, G. 1987, A&A, 182, 243
Matsakis, D. N., Evans, N. J., II, Sato, T., & Zuckerman, B. 1976, AJ, 81, 172
McCutcheon, W. H., Dewdney, P. E., Purton, C. R., & Sato, T. 1991, AJ, 101, 1435
Mead, K. N., Kutner, M. L., & Evans, N. J., II 1990, ApJ, 354, 492
Mihalas, D., & Binney, J. 1981, Galactic Astronomy (2d ed.; San Francisco: Freeman)
Miller, G. E., & Scalo, J. M. 1979, ApJS, 41, 513
Panagia, N. 1973, AJ, 78, 929
Rudolph, A. L., Simpson, J., Haas, M. R., Erickson, E. F., & Fich, M. 1996, in preparation
Sagar, R., Piskunov, A. E., Myakutin, V. I., & Joshi, V. C. 1986, MNRAS, 220, 383
Scalo, J. M. 1986, Fundam. Cosmic Phys., 11, 1
Shaver, P. A., McGee, R. X., Newton, L. M., Danks, A. C., & Pottasch, S. R. 1983, MNRAS, 204, 53
Simpson, J. P., Colgan, S. W. J., Rubin, R. H., Erickson, E. F., & Haas, M. R. 1995, ApJ, 444, 721
Stark, A. A. 1984, ApJ, 281, 624
Stark, A. A., & Brand, J. 1989, ApJ, 339, 763
Tarrab, I. 1982, A&A, 113, 57
Tenorio-Tagle, G. 1979, A&A, 71, 59
Wilson, T. L., & Matteucci, F. 1992, A&A Rev., 4, 1
Wink, J. E., Wilson, T. L., & Bieging, J. H. 1983, A&A, 127, 211
Wood, D. O. S., & Churchwell, E. 1989, ApJS, 69, 831 (WC)
Wouterloot, J. G. A., & Brand, J. 1989, A&AS, 80, 149 (WB89)
———. 1996, A&A, submitted
Wouterloot, J. G. A., Brand, J., Burton, W. B., & Kwee, K. K. 1990, A&A, 230, 21
Wouterloot, J. G. A., Brand, J., & Fiegle, K. 1993, A&AS, 98, 589
Wouterloot, J. G. A., Brand, J., & Henkel, C. 1988a, A&A, 191, 323 (WBH)
Wouterloot, J. G. A., Fiegle, K., Brand, J., & Winnewisser, G. 1995, A&A, 301, 236
Wouterloot, J. G. A., & Walmsley, C. M. 1986, A&A, 168, 237
Wouterloot, J. G. A., Walmsley, C. M., & Henkel, C. 1988b, A&A, 203, 367
Yorke, H. W., Tenorio-Tagle, G., & Bodenheimer, P. 1983, A&A, 127, 313